Cathodoluminescence of Nanocrystalline Y_2O_3:Eu^{3+} with Various Eu^{3+} Concentrations

Daniel den Engelsen, Paul Harris, Terry Ireland,[z] and Jack Silver[z]

Centre for Phosphor and Display Materials, Wolfson Centre for Materials Processing, Brunel University London, Kingston Lane, Uxbridge, Middlesex, UB8 3PH, United Kingdom

Herein a study on the preparation and cathodoluminescence of monosized spherical nanoparticles of Y2O3:Eu3+ having a Eu3+ concentration that varies between 0.01 and 10% is described. The luminous efficiency and decay time have been determined at low a current density, whereas cathodoluminescence-microscopy has been carried out at high current density, the latter led to substantial saturation of certain spectral transitions. A novel theory is presented to evaluate the critical distance for energy transfer from Eu3+ ions in S6 to Eu3+ ions in C2 sites. It was found that Y2O3:Eu3+ with 1–2% Eu3+ has the highest luminous efficiency of 16lm/w at 15keV electron energy. Decay times of the emission from 5D0 (C2) and 5D1 (C2) and 5D0 (S6) levels were determined. The difference in decay time from the 5D0 (C2) and 5D1 (C2) levels largely explained the observed phenomena in the cathodoluminescence-micrographs recorded with our field emission scanning electron microscope.

In a study of the cathodoluminescence (CL) of europium-doped yttrium oxide (Y_2O_3:Eu^{3+}) and zinc-doped zinc oxide (ZnO:Zn) we described both a new measuring method[1] and an idea to maximize the light output of single and multilayers of particles of these phosphors.[2] The phosphors used in these published studies were spherical nanoparticles of Y_2O_3:Eu^{3+} and micrometer sized ZnO:Zn particles. The spherical nanoparticles of Y_2O_3:Eu^{3+} were not monodisperse, because they consisted of a mixture of various batches. The objective of the continuation of our investigations that are reported herein was preparing and characterizing monosized spherical nanoparticles of Y_2O_3:Eu^{3+} with various concentrations of Eu^{3+}. In this work CL-techniques were used as the characterization method of choice: in a vacuum system equipped with an electron gun and spectrometers, and in a field emission scanning electron microscope (FESEM).[3]

The application of Y_2O_3:Eu^{3+} in cathode ray tubes has fostered extended luminescence studies of this material. Before 1996 these studies were focused mainly on micrometer sized particles,[4–12] more recently the attention has been directed to nano-sized powder materials.[13–19] In the earlier studies[4–12] the focus was on the interpretation of the excitation and emission spectra in terms of energy transfer in the Y_2O_3:Eu^{3+} crystals, whereas in the latter studies[13–19] the attention shifted toward the synthesis of nanomaterials. Most studies used photoluminescence (PL) techniques,[4–7] which enabled the excitation of energy levels having a particular symmetry and yielded insight on the energy flow in Y_2O_3:Eu^{3+}. Most studies on the CL of Y_2O_3:Eu^{3+} were limited to the evaluation of the luminous efficiency.[10–12]

A detailed investigation of the energy flow in Y_2O_3:Eu^{3+} after excitation by an electron beam was performed by Klaassen et al.[8] These authors also studied saturation effects in Y_2O_3:Eu^{3+} at high current densities in an electron microscope.[9] Although the work of Klaassen et al. is comprehensive and extensive, it was considered worthwhile to investigate the CL-spectra at low current density and the decay behavior of Y_2O_3:Eu^{3+} at low and high current densities using a different method of analysis. Moreover, Klaassen et al. did not indicate which spectral transitions they selected for their analyses. This selection is not trivial, because many peaks in the spectrum of Y_2O_3:Eu^{3+} suffer from overlap or are combinations of more than one spectral transition.[5,6]

The first phase in the energy flow in Y_2O_3:Eu^{3+} after excitation of the Y_2O_3 lattice by an electron beam is charge transfer by exciting the Eu^{3+} ions. Then fast radiationless relaxation to the various ^5D_J levels of Eu^{3+} takes place. From these levels light is emitted. How the various ^5D_J levels are populated will not be addressed, but rather

limit the study to the energy transfer between Eu^{3+} ions in the two crystallographic sites. Pure and Eu^{3+} doped Y_2O_3 crystals have the cubic structure of the mineral bixbyite with 16 Y_2O_3 molecules in one cell.[4,20] In Y_2O_3 there are two different Y^{3+} lattice sites, which possess the point symmetries C_2 and S_6 (Schoenflies notation): 24 lattice sites have C_2 symmetry, while the other 8 have S_6 symmetry. Both sites are six coordinate and are thus present in the ratio of 3:1. The sites are presented in Figure 1. Upon doping Y_2O_3 with Eu^{3+} these lattice sites are occupied with Eu^{3+} with almost equal probability.[4]

Heber et al.[4] and Buijs et al.[7] derived from PL-measurements of Y_2O_3:Eu^{3+} with various Eu^{3+} concentrations and at various temperatures respectively that after excitation of a crystal with high Eu^{3+} concentration, energy can be transferred from S_6 states to C_2 states. At low Eu^{3+} concentration there is no interaction between a Eu^{3+} ion at a S_6 site and a Eu^{3+} ion at a C_2 site respectively and thus, there will be no energy transfer. Energy transfer also occurs in phosphors that are excited by an electron beam; therefore, it was also an objective of this work to investigate what information concerning energy transfer can be obtained from CL-spectra that are generated without activation of specified energy levels.

In a review entitled "*Probes of Structural and Electronic Environments of Phosphor Activators: Mossbauer and Raman Spectroscopy*" we commented on work reported on commercial Y_2O_3:Eu^{3+} phosphors.[21] This work showed that in Y_2O_3:Eu^{3+}, having an Eu^{3+} concentration of ca. 4.7 mole %, efficient energy transfer occurs between the S_6 and C_2 sites for Eu^{3+} in the $^5D_0$ level. As the $^5D_0$ level in the S_6 site is 87 cm^{-1} higher than the same level in the C_2 site, the efficient energy transfer from S_6 to C_2 sites presumably occurs by simultaneous creation of a phonon.[22] This efficient energy transfer is necessary for the high emission efficiency of the Y_2O_3:Eu^{3+} phosphor, as the $^5D_0 \rightarrow ^7F_2$ transition which gives rise to the red 611 nm emission is electric dipole allowed for Eu^{3+} in C_2 sites but forbidden for Eu^{3+} in S_6 sites.

In this work it was decided to focus on the $^5D_0 \rightarrow ^7F_1$ (S_6) transition at 582 nm and the $^5D_0 \rightarrow ^7F_2$ (C_2) transition at 611 nm, because these are reasonably well separated from other transitions[6] and allow luminescence decay measurements that are not perturbed by a large overlap of nearby transitions. Another important condition for this selection was the radiance of the $^5D_0 \rightarrow ^7F_1$ (S_6) transition at 582 nm, which was sufficient to perform decay measurements at room temperature.

The outline of this paper is as follows. In the experimental section the synthesis of monosized spherical Y_2O_3:Eu^{3+} nanoparticles, the deposition of thin films and the measuring methods are described. Results and discussions thereof are presented in the subsequent section. The final section contains the conclusions.

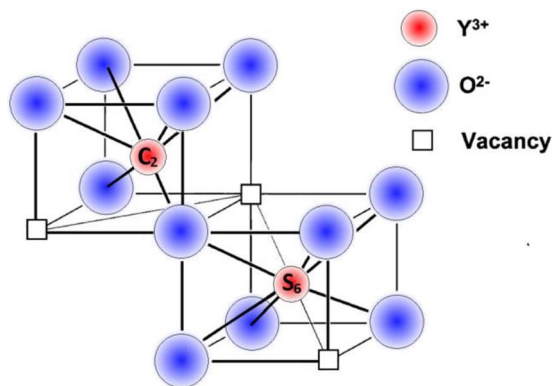[z]E-mail: jack.silver@brunel.ac.uk; terry.ireland@brunel.ac.uk

Figure 1. C_2 and S_6 sites of the Y^{3+} cation in cubic Y_2O_3. These sites have vacancies on a face diagonal and a body diagonal, respectively.

Experimental

Materials.— Yttrium oxide (99.99%) and europium oxide (99.99%) were obtained from Ampere Industrie, France; urea, nitric acid and isopropanol (IPA) were supplied by Fisher Scientific, UK., all chemicals were used as received. Glass substrates (1 cm^2) coated with an indium tin oxide (ITO) film (85Ω/sq) were obtained from Visiontek Ltd., UK. Aluminum pin stubs for the FESEM studies were polished before cleaning. The ITO and aluminum pin stubs were carefully cleaned in de-ionised water and IPA using ultrasonic cavitation. Conductive carbon tabs coated with adhesive on both sides were also used for the attaching samples for FESEM imaging studies.

Synthesis of monosized spherical Y_2O_3:Eu^{3+} nanoparticles.— The synthesis of monosized spherical Y_2O_3:Eu^{3+} nanoparticles by the urea method has been described extensively in our earlier work.[1,13,23] Since the aim was synthesizing particles with a diameter of about 225 nm after annealing at high temperature, the aging of the turbid suspensions for all samples was continued for one hour at 90°C. This aging time essentially determined the diameter of the spherical particles.

Sample preparation.— Thin films of monosized spherical Y_2O_3:Eu^{3+} nanoparticles (2mg/cm^2) were deposited onto ITO-substrates by electrophoresis from an IPA suspension for the luminance studies. Previously we have reported[1] that deposition of Y_2O_3:Eu^{3+} by electrophoresis from an IPA-suspension to which 37.5 mg Mg(NO$_3$)$_2$ (for 500ml IPA) was added to induce charging of the Y_2O_3:Eu^{3+} particles which led to layers that were non-uniformly coated and therefore produced considerable light scattering. Although the addition of Mg(NO$_3$)$_2$ is generally recommended for electrophoretic deposition of phosphor particles onto conductive substrates,[24] by omitting Mg(NO$_3$)$_2$ it was possible to deposit uniform layers that had no excessive light scattering. Thus, it may be concluded that by not adding Mg(NO$_3$)$_2$ the Debye layer surrounding the nanoparticles was large enough to prevent agglomeration of the particles, while the charging of the particles was sufficient to enable an acceptable coating time of about 2 minutes.

Measuring methods.— The morphology and particle size assessment of the phosphor powders were undertaken using a FESEM, Supra 35 VP, Carl Zeiss, Germany.

The microscope is equipped with four detector systems as shown in Figure 2. The first is an Everhart-Thornley (ET) SE detector, which collects primarily secondary electrons (SEs), although some backscattered electrons (BSEs) may also contribute.

There is also an in-lens SE detector, for use when a very short working distance is required, and this detects only SEs. An annular (retractable) Robinson solid state BSE detector is mounted immediately above the sample. The microscope has also a facility to collect CL generated by the electron beam when it hits a phosphor. After amplification of these light signals in a photomultiplier high quality panchromatic CL-images of phosphor materials can be obtained. We have used this facility to study the decay behavior of Y_2O_3:Eu^{3+}. Image analysis of the panchromatic CL-micrographs was performed using ImageJ (Public Domain) software. CL micrographs are represented in shades of grey; they are therefore called panchromatic. The gray shade G(i,j) in a CL graph, where i and j indicate a pixel in the ith row and jth column, can be written as:

$$G(i, j) = V(i, j) \int_{\lambda 1}^{\lambda 2} P(i, j)s(\lambda)d\lambda \qquad [1]$$

where V(i,j) is a geometrical factor representing the viewing factor of the pixel i,j to the optical detector. From this definition it follows that V(i,j) also takes care of shadowing effects caused by other particles. P(i,j) is the power spectrum of the material at pixel i,j and s(λ) is the sensitivity of the photocathode of the photomultiplier. The integration is made between the minimum and maximum wavelengths of s(λ). From Eq. 1 it is immediately clear that the greyscale in a CL-micrograph is not equal to the radiance, since P(i,j) is convoluted with s. The term G(i,j) is also a function of time, because of decay of the fluorescence (or phosphorescence). If the decay time is more than 4 orders of magnitude smaller than the scan rate (in frame/s), there will no smearing effect visible in the CL-micrograph. For longer decay times, smearing will be visible. The Zeiss Supra FESEM is provided with scan rates of 1.7s (ss12) to 0.12ms (ss1) per line and this defines the range of materials that can be studied. For weakly luminescent materials and/or the highest scan speeds the images can be repeatedly scanned and averaged to improve the signal to noise.
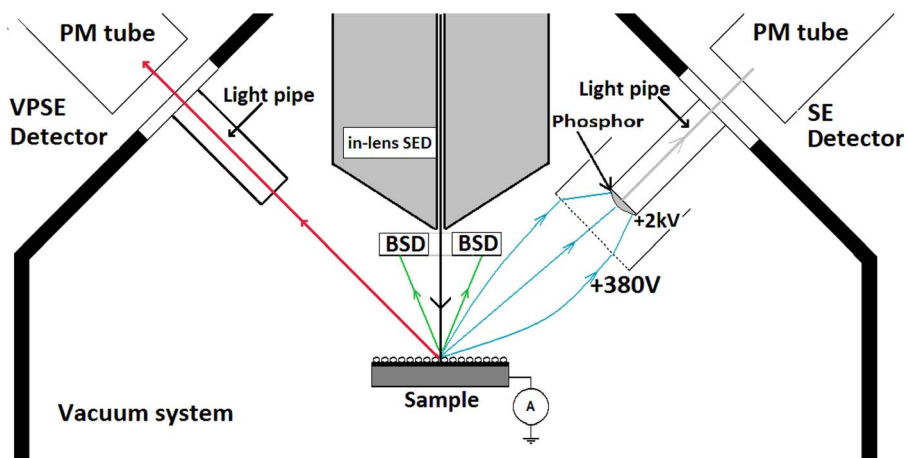

Figure 2. Arrangement of detectors in Zeiss Supra 35VP. VPSE detector is the variable pressure detector that collects and amplifies CL-signals at high vacuum condition. BSD stands for backscatter detector. SE-detector is an Everhard-Thornley detector. The position of the in-lens SE detector is also indicated.
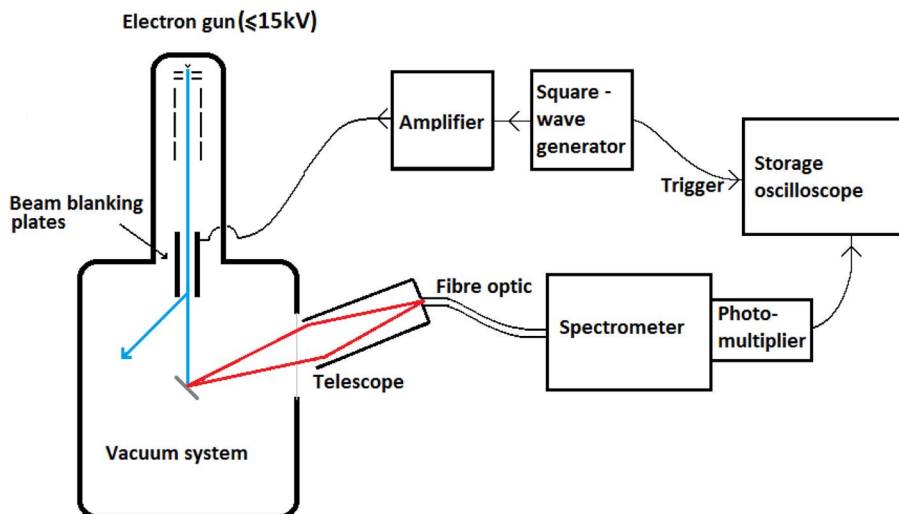
Figure 3. Measuring system for decay of spectral transitions. The spectrometer used in this system was a Bentham monochromator.

The CL measurements for luminous efficiency and decay times were carried out in two different high vacuum chambers at a vacuum level of $\approx 3 \times 10^{-6}$ mbar using Kimball Physics Inc., USA, electron guns and associated power supplies over the ranges of electron beam voltages of 1–5 kV and 3–15 kV respectively. The electron guns had the ability to focus and defocus the beam over a range of current densities. For the studies of the luminous efficiency a uniform electron beam by defocusing and a current density of $1\mu A/cm^2$ was used. Deflection plates enabled optimum positioning of the electron beam on the sample and a ZnO:Zn reference. The latter being a non-charging thin film of ZnO:Zn powder on ITO to adjust the current on the charging Y_2O_3:Eu^{3+} samples as explained in our previous work.[1,2]

For the determination of the luminous efficiency, spectral radiance and luminance were recorded with two Spectrobos 1200 spectroradiometers manufactured by JETI, Germany, between 380 and 780 nm in reflection and transmission mode.[1,2] High resolution spectra (± 0.1 nm) were also recorded with a Bentham, UK, monochromator detector system between 350 and 800 nm. By blanking the E-beam of the Kimball electron gun we could measure the persistence behavior of various spectral transitions in Y_2O_3:Eu^{3+}. The measuring system is schematically indicated in Figure 3.

The blanking speed was in the order of nano-seconds, orders of magnitude smaller than the decay times of the spectral transitions of Y_2O_3:Eu^{3+}. The Bentham monochromator was used to tune the measuring wavelength to the maximum radiance of a particular spectral transition. Pulse frequency of the beam blanking system was 10Hz. All measurements were performed at room temperature (298 K).

Results and Discussion

FESEM characterisation.— Figure 4 represents a FESEM micrograph of monosized spherical Y_2O_3:Eu^{3+} particles forming a film electrophoretically deposited onto ITO coated glass slide. The particles are approximately 220 nm in diameter and form a highly dense layer with a low concentration of voids. As proof as to the monodispersity of the particles, when a solution is allowed to evaporate, a glass–like thick film is formed that displays a weak opalescence (which is determined by the diameter of the spherical particles and the close packing producing a modulation of the refractive index, as occurs in three-dimensional photonic bandgap crystals) as indeed this material formed has the optical characteristics of a bare opal.

Cathodoluminescence spectra.— Figure 5 shows CL spectra of films of monosized spherical Y_2O_3:Eu^{3+} nanoparticles excited by an electron beam of 15keV at a current density of 3 $\mu A/cm^2$ and temperature of 298 K. The spectra are normalized to 100 arbitrary units for the $^5D_0 \rightarrow {}^7F_2$ (C$_2$) transition at 611nm to indicate what trends can be

observed for the weaker spectral transitions. For reasons of clarity the spectra with 10%, 4%, 3%, 0.8 and 0.5 mole percent europium have not been inserted in Figure 5. The inset of Figure 5 shows the wavelength range between 570 and 605nm in more detail. The strongest effect can be observed for the $^5D_0 \rightarrow {}^7F_{1a}$ (S$_6$) transition at 582nm. The radiance is weak at 5% Eu^{3+} and increases by about a factor of 4 for low Eu^{3+} concentrations. The same behavior can be observed for the transition at 592 nm, although the effect is smaller than for the $^5D_0 \rightarrow {}^7F_{1a}$ (S$_6$) transition. The peak at 592 nm is a combination of two transitions, viz. $^5D_0 \rightarrow {}^7F_{1b}$ (S$_6$) and $^5D_0 \rightarrow {}^7F_{1b}$ (C$_2$) as was found by Hunt and Pappalardo:[6] this explains that the increase of the normalized radiance of this peak at low Eu^{3+} concentration is less than for the 582 nm peak. The spectrum of Y_2O_3:Eu^{3+} with 0.01% Eu^{3+} exhibits a weak emission peak at 572 nm, shown in the inset of Fig 5. This emission line cannot be assigned to any energy transition of Y_2O_3:Eu^{3+}. It is therefore, confidently assigned to dysprosium contamination in the Y_2O_3 material used for the synthesis. Dysprosium has its main luminescence line at 572.5nm which is due to the $^7F_{9/2} \rightarrow {}^6H_{15/2}$ transitions; this main transition is not exhibited by the other lanthanides. The high purity yttrium oxide used in this work has a number of lanthanide contaminants at the parts per million concentration level. During our measurements a weak Gd^{3+} peak was observed at 314 nm (not shown in the spectra of Fig 5), which was also reported by Tanner et al.[19] Since this Gd^{3+} transition was out of the range of interest of this work and any (very) low intensity peaks
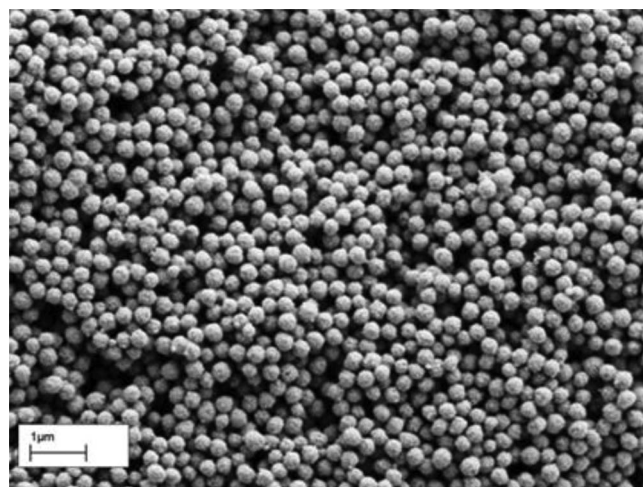

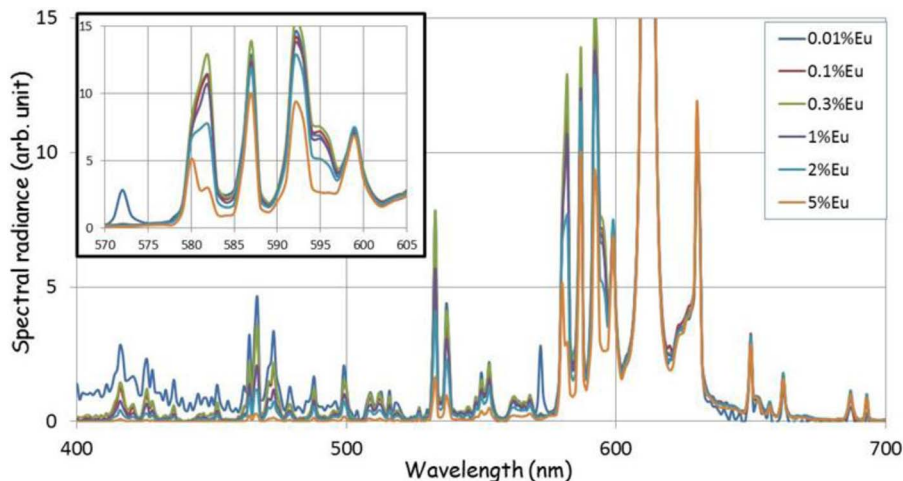**Figure 4.** FESEM micrograph of a film of Y_2O_3:Eu^{3+} (0.1 Mol% Eu) on ITO-substrate at 3keV beam energy.

Figure 5. CL spectra of Y_2O_3:Eu^{3+} at various europium mole fractions. Beam energy 15keV, current density 3 $\mu A/cm^2$. Spectra are normalized to 100 arbitrary units for the $^5D_0 \rightarrow ^7F_2$ (C_2) transition at 611nm.

of other lanthanide contaminants are hidden under the much stronger Eu^{3+} transitions, we assume that these contaminants do not affect the results of this study.

We shall now present a consideration on the energy transfer from Eu^{3+} in S_6 to Eu^{3+} in C_2 as described by others based on PL studies.[4–8] As mentioned before, the $^5D_0 \rightarrow ^7F_1$ (S_6) transition at 582 nm and the $^5D_0 \rightarrow ^7F_2$ (C_2) transition at 611 nm were selected for this study. The first step is determining the ratio between these two transitions: R_{611}/R_{582}. Figure 6 shows a deconvolution of the spectra around 582 and 611nm: this deconvolution enables a determination of the radiances, R_{582} and R_{611}.

It was assumed that the spectral transitions have Lorentzian shapes. The spectral radiance SR(λ), where λ represents the wavelength, can be written as:

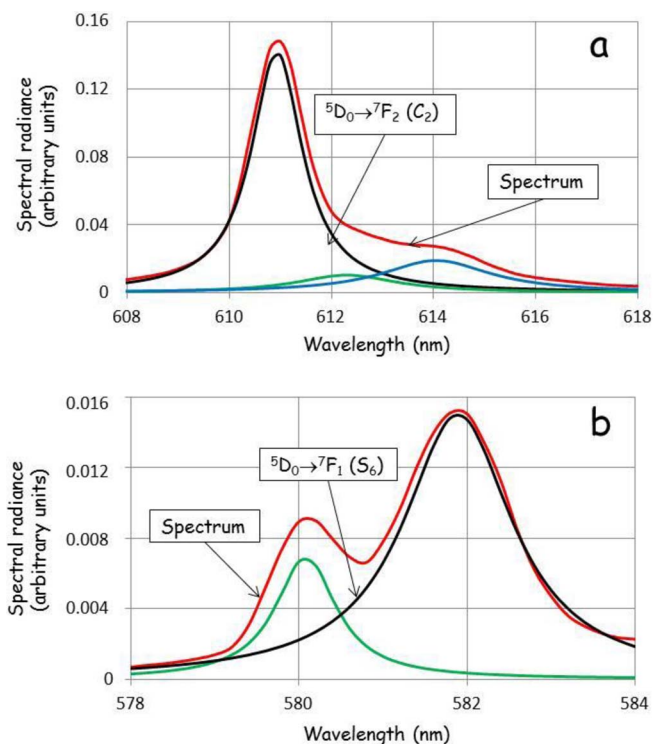$$SR(\lambda) = \sum_i \frac{A_i}{1 + \frac{(\lambda - \lambda_i)^2}{b_i^2}} \quad [2]$$

Figure 6. Deconvolution of parts of the CL spectrum of Y_2O_3:Eu^{3+} (0.8 mole % Eu) at 15kV and 2$\mu A/cm^2$. (a) 611 nm region, (b) 582 nm region.

where A_i is the maximum spectral radiance of the ith peak, λ_i is the wavelength for the maximum and b_i is the half width at half maximum. The radiance of the ith transition is:

$$R_i = \int_{-\infty}^{\infty} \frac{A_i d\lambda}{1 + \frac{(\lambda - \lambda_i)^2}{b_i^2}} = A_i \pi b_i \quad [3]$$

The relevant transitions are indicated in Figures 6a and 6b. Figure 6 indicates that the full width at half maximum (FWHM) of the 611 nm transition is smaller than that of 582 nm: viz. $FWHM_{611}$ = 1.22 nm and $FWHM_{582}$ =1.58 nm. For both transitions the FWHMs did not change as a function of Eu^{3+} concentration. It is assumed that the ratio R_{611}/R_{583} is a relevant indicator of the energy flow from S_6 to C_2 sites at short distances between Eu^{3+} ions. The spectra represented in Figures 6a and 6b have also been deconvoluted with Gaussian peaks; for this deconvolution an extra peak was necessary for both spectral regions. The result of this convolution led to $\approx$33% lower values of the ratio R_{611}/R_{583}; however, the essential results and conclusions were the same.

Figure 7 shows two different plots of the radiance ratio R_{611}/R_{582}: Figure 7a is a plot of this ratio versus the Eu^{3+} concentration and Figure 7b is plot of the ratio versus the average distance D_{Eu} between the Eu^{3+} ions in the Y_2O_3 lattice. This average distance in the cubic lattice is calculated according to:

$$D_{Eu} = \sqrt[3]{\frac{100M}{2\rho Nc}} \quad [4]$$

where M is the molecular weight of Y_2O_3, ρ is the density of Y_2O_3, being 5.01 g/cm^3, and N is Avogadro´s number. The factor 100 appears in Eq. 4, because c is expressed in %.

If all Y^{3+} ions in the Y_2O_3 lattice would have been changed for Eu^{3+} ions, the average distance between the Eu^{3+} ions is 0.334 nm according to Eq. 4. In the Y_2O_3 lattice the shortest distance between the cation sites C_2 and S_6 is 0.352 nm;[4] so, it can be concluded that Eq. 4 is a fair representation of the average distance between an Eu^{3+} ion at a S_6 site and an Eu^{3+} ion at a C_2 site as a function of the Eu^{3+} concentration.

Figures 7a and 7b show that the radiance ratio R_{611}/R_{582} is essentially constant in the range between 0.01 and 0.5% Eu^{3+}.

The diamonds in Figures 7a and 7b represent the experimental results obtained with the algorithm described in Eqs. 2 and 3; the dashed curves are best fits to these results.

These curves can be represented by the following phenomenological equations:

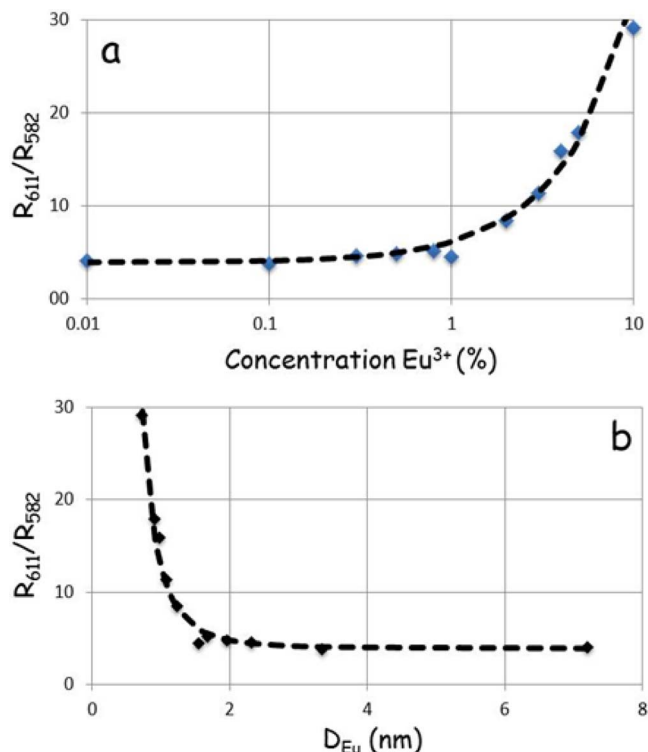$$\frac{R_{611}}{R_{582}} = G + H_1 c^\delta \quad [5a]$$

Figure 7. (a) Radiance ratio R_{611}/R_{582} versus mole fraction of europium in $Y_2O_3:Eu^{3+}$. (b) Radiance ratio R_{611}/R_{582} versus $Eu^{3+} : Eu^{3+}$ distance in the Y_2O_3 lattice.

and

$$\frac{R_{611}}{R_{583}} = G + H_2 D_{Eu}^{-3\delta} \qquad [5b]$$

The parameters G and δ in Eqs. (5a) and (5b) respectively have the same values; so, the exponent of D_{Eu} in Eq. (5b) is 3 times larger than then the exponent of the concentration c in Eq. (5a), because of Eq. 4. The values of G, H_1, δ and H_2 are 5.8, 2.9, 1.1 and 14 respectively. Since the steepness of the fitted curve in Figure 7b is larger than that in Figure 7a it allows a better estimate of the knee point of the curve, being 1.7 nm. In Figure 7a this would be equivalent to a concentration of 0.8 mole % Eu^{3+}. In other words, the critical distance, crit D_{Eu}, for interaction between the S_6 and C_2 sites is 1.7nm.

In the literature one usually defines a parameter R_0, being the critical transfer distance, for which the transfer rate of energy from S_6 to C_2 is equal to the radiative decay rate.[7] Values published for R_0 of Eu^{3+} cations in the cubic Y_2O_3 are 0.87 nm,[4] 0.82 nm[7] and 0.86 nm.[25] By constructing two spheres both with a radius of R_0, the first centered at an S_6 site and the second centered at a C_2 site, energy transfer from S_6 to C_2 is possible when the spheres overlap. With this picture in mind it is easy to conclude that the critical distance D_{Eu} as concluded from Figure 7b, is equal to $2R_0$; so, we get R_0=0.85 nm, which matches well with the published values of R_0.

From this straightforward spectral analysis it can be concluded that an evaluation of the critical energy transfer distance is possible without extensive analyses on the decay of the emission at various temperatures (which is the most used method of evaluation). Klaassen et al.[8] also presented the relative intensity from excited ^5D_J levels to the ^7F_J-multiplets under stationary electron bombardment at low current density as a function of the Eu^{3+} concentration. Although their highest Eu^{3+} concentration was only 1%, the knee in their simulated curve was at ≈0.3% Eu^{3+}, slightly different from our result. The analysis of Klaassen et al. was based on the evaluation of radiative decay times and non-radiative decay rates.

Luminous efficiency.— Thin films of $Y_2O_3:Eu^{3+}$ mono-sized particles deposited on ITO coated glass slides were used for measuring the luminance and spectral radiance. The weight of the $Y_2O_3:Eu$ films was 2 mg/cm². From Figure 4 it can be concluded that the monosized spherical $Y_2O_3:Eu^{3+}$ nanoparticles had a random close packing, although there were areas with a higher packing density. Random close packing gives a packing density of 0.64. The film thickness F is calculated using a packing density of 0.65, slightly larger than 0.64, with:

$$F = \frac{W}{\rho B} \qquad [6]$$

where W is the coating weight, ρ is the density of crystalline phosphor material, 5.0 g/cm³ for $Y_2O_3:Eu^{3+}$, and B is the packing density in the layer.[1] With these values for W, ρ and B the film thickness F is 6.2μm. The penetration depth of 15keV electrons in crystalline Y_2O_3 is 1.9μm²; so, it can safely be assumed that the electron energy is absorbed for more than 99% in the phosphor layer.

Figure 8a represents the luminous efficiency calculated from the luminance measured in the transmission and reflection modes; for reasons of clarity not all data have been inserted in the graph. The evaluation method for the luminous efficiency has been indicated in detail in our previous work.[1,2] It can be seen that the luminous efficiency is essentially constant between 7 and 15 kV. In Figure 8b the luminous efficiency is plotted as a function of the mole fraction of Eu. The results of Yang et al.,[11] which are also plotted in Figure 8b, refer to micrometer sized $Y_2O_3:Eu^{3+}$ particles and measurements at 4kV.

From our data represented in Figure 8b it can be concluded that between 1 and 2% mole % Eu^{3+} in Y_2O_3 the maximum luminous efficiency of ≈16 lm/w at 15 keV electron energy is obtained. This corresponds to an energy efficiency of 5.2%. This result is higher than we found before.[2] The reason for the rather low efficiency in[2] was the non-uniformity of the settled layers: especially in the center area of the ITO substrate the films were thinner and it is assumed that not all electron energy was transferred to the phosphor at high beam energy. In the present study the quality of the electrophoretic layers is better, as
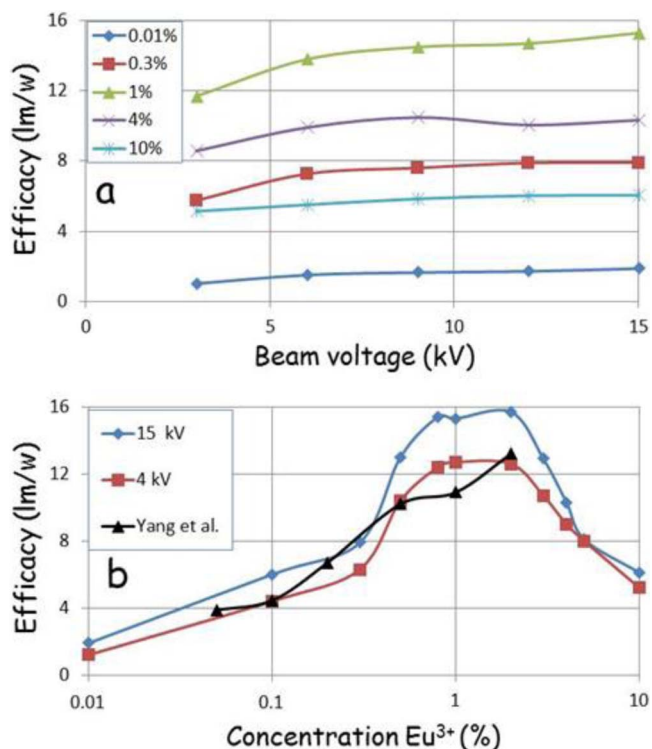

Figure 8. (a) Luminous efficacy as a function of the voltage of the electron beam. (b) Luminous efficacy as a function of Eu^{3+} mole fraction at 4 and 15kV. The results of Yang et al.[11] at 4kV are also plotted.
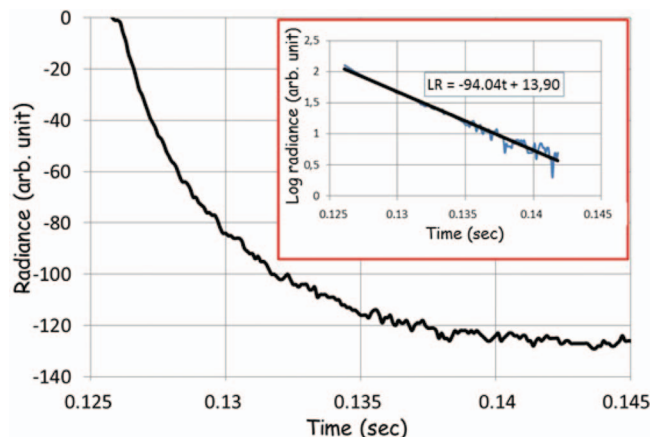
Figure 9. Decay curve of $Y_2O_3:Eu^{3+}$ 2%: $^5D_0 \rightarrow ^7F_{1a}$ (S_6) transition at 582 nm. The inset shows the logarithm of the radiance (LR) as a function of time.

shown in Figure 4. Jiang et al.[14] found that nanocrystalline $Y_2O_3:Eu^{3+}$ excited by an electron beam had the highest luminous efficiency at an Eu^{3+} concentration of 2.5%. For nanocrystalline $Y_2O_3:Eu^{3+}$ with 2% Eu^{3+} they evaluated a luminous efficiency of 11.5lm/w at 4keV beam energy from the measurement of the luminance in the reflection mode only. Our results provide a value of 12.6 lm/w at 4keV, which is slightly larger than the result of Jiang et al.

Finally it was noted that the highest efficiency of $Y_2O_3:Eu^{3+}$ nanoparticles with 2% Eu^{3+} is about 30% lower than that of micrometer sized $Y_2O_3:Eu^{3+}$ particles.[10] It is well known that the CL efficiency of nanoparticles is smaller than that of the corresponding micrometer sized particles.[11,13] This effect is usually attributed to the surface, which is much larger for nanoparticles than for micrometer particles.

Decay.— Thin films of monosized spherical $Y_2O_3:Eu^{3+}$ nanoparticles were excited with a defocused electron beam of 15kV and current density of $3\mu A/cm^2$. Saturation did not occur at this current density under stationary conditions, as will be shown in the next section on the observations in the FESEM. A typical decay curve is presented in Figure 9.

With a blanking frequency of 10Hz the time for the beam on was 50 ms, which is much longer than the reported decay times of $Y_2O_3:Eu^{3+}$.[8] So, it can be assumed that the energy flow in the $Y_2O_3:Eu^{3+}$ nanoparticles was in a steady state at switching off the electron beam.

The decay curves recorded during this study can be represented by a single exponential function. The time constant τ of the decay has been evaluated from a log plot of the decay curve shown in the inset of Figure 9. In some cases a correction for the background has been applied. The inset in Figure 9 shows the algebraic representation of the regression line. From the coefficient before the parameter t the non-corrected time constant can be calculated according to 434.4/94.04=4.6 ms. From this value an equipment correction of 0.3ms must be subtracted to get the time constant of the $^5D_0 \rightarrow ^7F_{1a}$ (S_6) transition.

Table I shows the time constants in ms for the various spectral transitions and samples measured during this investigation. The accuracy for the $^5D_0 \rightarrow ^7F_2$ (C_2) transition at 611nm is about ±3%. For the other spectral transitions the accuracy is between ±5 and ±10%. The S_6 transitions are magnetic dipole transitions and it is therefore expected that the time constant of the decay is longer than for corresponding (allowed) C_2 transitions. This behavior is reflected in the time constants listed in Table I. The time constant of the $^5D_0 \rightarrow ^7F_2$ (C_2) transition is shorter than that of the $^5D_0 \rightarrow ^7F_{1a}$ (S_6) transition, while the mixed peak at 592nm has an intermediate value, because it is made up of a combination of a C_2 and S_6 transition, as indicated before. The $^5D_1 \rightarrow ^7F_1$ (C_2) transition at 533 nm has a much shorter

Table I. Decay times (in ms) of $Y_2O_3:Eu^{3+}$ with different Eu concentration measured at 15keV and current density of $\approx 3\mu A/cm^2$.

Eu^{3+} (%)	$^5D_0 \rightarrow ^7F_2$ (C_2) (611 nm)	$^5D_0 \rightarrow ^7F_1$ (S_6) (582 nm)	$^5D_0 \rightarrow ^7F_1$ (C_2/S_6) (592 nm)
10	0.70	1.0	0.77
5	0.92	1.8	1.2
4	0.96	2.6	1.5
3	1.03	3.4	1.6
2	1.06	4.3	1.7
1	1.05	4.8	1.7
0.8	1.02	5.8	1.7
0.5	1.03	6.5	2.5
0.3	1.02	5.6	1.7
0.1	0.95	4.5	
0.01	0.99		

time constant, $<50\,\mu s$. Because of the limitations of our equipment, it was not possible to measure an accurate value for this time constant.

The time constants vary as a function of Eu^{3+} concentration: for the $^5D_0 \rightarrow ^7F_2$ (C_2) transition at 611 nm; they stabilize at 1.02 ms for concentrations $<1\%$ Eu^{3+}. Klaassen et al.[8] also observed in their PL-experiments that time constants of the transitions in $Y_2O_3:Eu^{3+}$ with high Eu^{3+}-concentration are smaller than those with lower Eu^{3+} concentrations; they attributed this effect to concentration quenching. According to their analysis, the reciprocal time constant $1/\tau$ can be written as:

$$1/\tau = 1/\tau_r + Ac^\gamma \qquad [7]$$

where τ_r is the radiative time constant and the second term represents the radiationless decay rate, c is the concentration of Eu^{3+} in % and A and γ are parameters that are fitted to the measured time constants .

The data listed in Table I are visualized in Figures 10a and 10b: as a function of Eu^{3+} concentration and as function of the average Eu^{3+} : Eu^{3+} distance in the $Y_2O_3:Eu^{3+}$ lattice respectively.

From Figures 10a and 10b it can be concluded that the radiative decay time for $^5D_0 \rightarrow ^7F_2$ (C_2) is 1.04 ms and for $^5D_0 \rightarrow ^7F_1$ (S_6) it is 5.4 ms, which is in fair agreement with the results of Klaassen et al.[8] By inserting Eq. 4 in (7) we get:

$$1/\tau = 1/\tau_r + A^* D_{Eu}{}^{-3\gamma} \qquad [7a]$$

Figure 10b shows $1/\tau$ versus D_{Eu}, which is the average Eu^{3+} : Eu^{3+} distance in $Y_2O_3:Eu^{3+}$, (depending on the tri-positive europium concentration in the yttrium oxide host lattice) for the $^5D_0 \rightarrow ^7F_2$ (C_2) transition at 611 nm and the $^5D_0 \rightarrow ^7F_1$ (S_6) transition at 582 nm. The parameters used for the calculation of the dashed curves in Figure 10b are listed in Table II. It can be seen in Table II that 3γ is 6 for $^5D_0 \rightarrow ^7F_2$ (C_2) and 5.8 for $^5D_0 \rightarrow ^7F_1$ (S_6): the exponent of D_{Eu} in Eq. (7a) is $\approx$ -6 for both transitions. So, it can be concluded that dipole-dipole interaction for both transitions causes the decrease of the decay time at higher Eu^{3+} concentrations. The difference between the two curves is the value of the factor A^*, which is much larger for the $^5D_0 \rightarrow ^7F_1$ (S_6) transition.

Table III shows a comparison of the time constants of decay curves of $Y_2O_3:Eu^{3+}$ of various transitions measured by other workers. The agreement is satisfactory, although it is difficult to draw conclusions on the concentration effect of Eu^{3+} in $Y_2O_3:Eu^{3+}$, because its concentration is not always stated in the references cited in Table II.

FESEM observations.— Figure 11 shows FESEM images of monosized spherical $Y_2O_3:Eu^{3+}$ nanoparticles on a polished aluminum pin stub (the polishing features can clearly be observed). Aluminum pin stubs were chosen to reflect some of the light generated in the particles in order to maximize the photon collection in the light pipe of the variable pressure secondary electron (VPSE) detector as indicated in Figure 2. Figures 11a and 11b are images of the same area, Figure 11a is the SE-micrograph and 11b is the
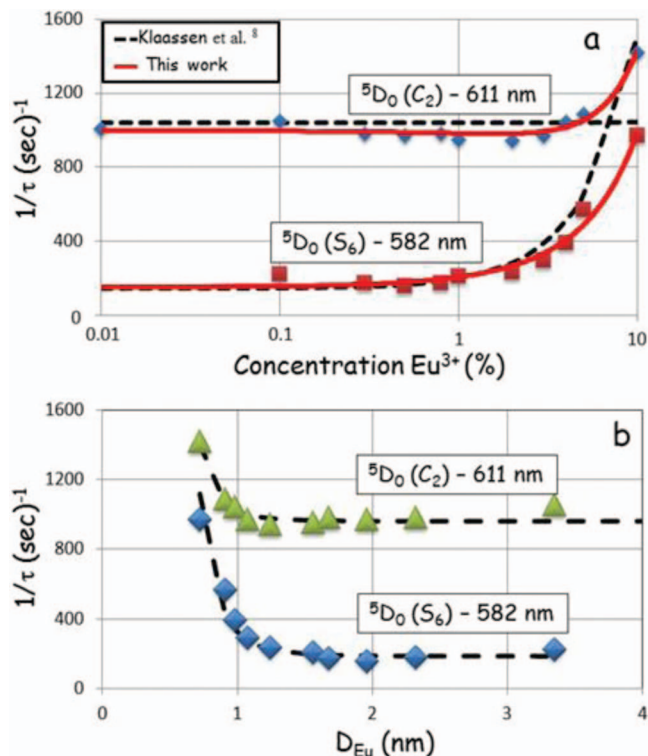
Figure 10. Reciprocal time constants for the $^5D_0 \rightarrow ^7F_2$ (C_2) transition at 611 nm and $^5D_0 \rightarrow ^7F_1$ (S_6) transition at 582 nm plotted versus Eu^{3+}-concentration in (a), and versus Eu^{3+} : Eu^{3+} distance in (b). Triangles and diamonds are experimental results; dashed curves in b are calculated according to Eq. 7a. The results of Klaassen et al.[8] are also represented in (a).

Table II. Parameters for decay curves represented in Figure 10b.

Parameter	$^5D_0 \rightarrow ^7F_{1a}$ (C_2) (611 nm)	$^5D_0 \rightarrow ^7F_1$ (S_6) (582 nm)
$1/\tau_r$ (ms)	1.04	5.4
$A*$	62	140
γ	2.0	1.9

CL-micrograph. The SE-micrograph is a clear picture and shows details of the particles, whereas in the CL-micrograph the nanoparticles are smeared out in the horizontal direction and show a comet-like tail. The reason for this blurring is the decay of CL in Y_2O_3:Eu^{3+}. So, the smearing of CL-images offers the opportunity to measure decay times of CL-phosphors.[3] Figure 11b shows a halo effect, which is particularly visible for clusters of Y_2O_3:Eu^{3+} nanoparticles. The halo is caused by BSEs emitting from the aluminium-substrate positions around the Y_2O_3:Eu^{3+} nanoparticles or clusters. These BSEs may also hit the phosphor nanoparticle and since the energy of the BSEs is large enough, CL is generated.
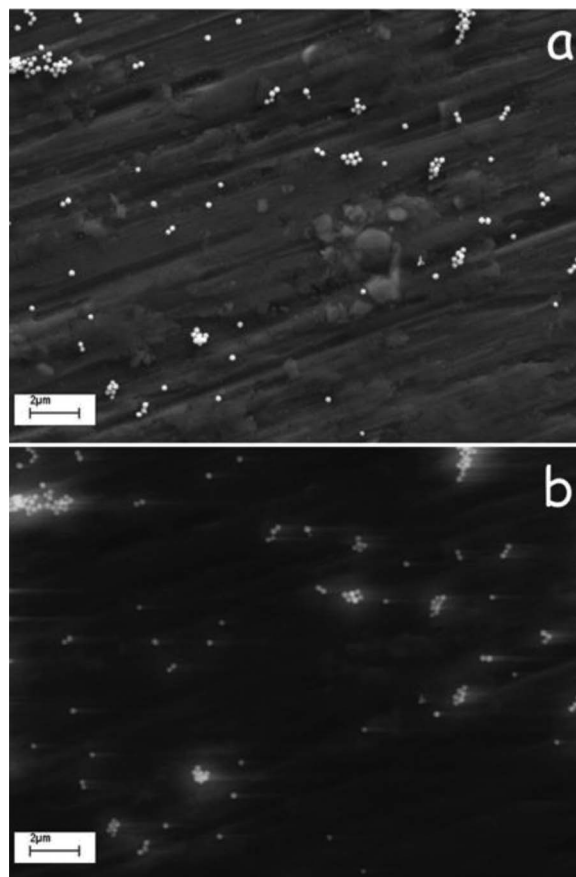

Figure 11 (a) SE-micrograph of Y_2O_3:Eu^{3+} (2% Eu^{3+}) nanoparticles on an Al-substrate. Beam energy: 10keV. b: CL-micrograph of the same area and same beam energy. Recorded at 20.2 seconds/frame.

Figure 12 summarizes the most important feature of the CL-micrographs, viz. that the smearing out in the horizontal direction decreases and virtually disappears for Y_2O_3:Eu^{3+} nanoparticles with low Eu^{3+} concentration. The decay curves of some individual nanoparticles have been analyzed with ImageJ software and the results are summarized in Table IV. Table IV shows that the time constant decreases at low Eu^{3+} concentration. At 0.1 and 0.01% Eu^{3+} no horizontal tail can be observed for a dwell time of 260µs per nanoparticles. However, by decreasing the dwell time to 2.5µs, the tail becomes visible again as shown in Figure 12.

The results presented in Figure 12 and Table IV will be interpreted in terms of saturation of the CL. The parameters that determine the degree of saturation under electron bombardment, i.e. loss of efficiency, are current density j, activator concentration c, time constant τ of the spectral transition and duration of the pulse Δt in non-stationary conditions. [8,9] Let us first consider the current density in the electron microscope. In focused condition the spot size of the electron beam

Table III. Comparison of time constants (in ms) of luminescence decay of Y_2O_3:Eu^{3+}.

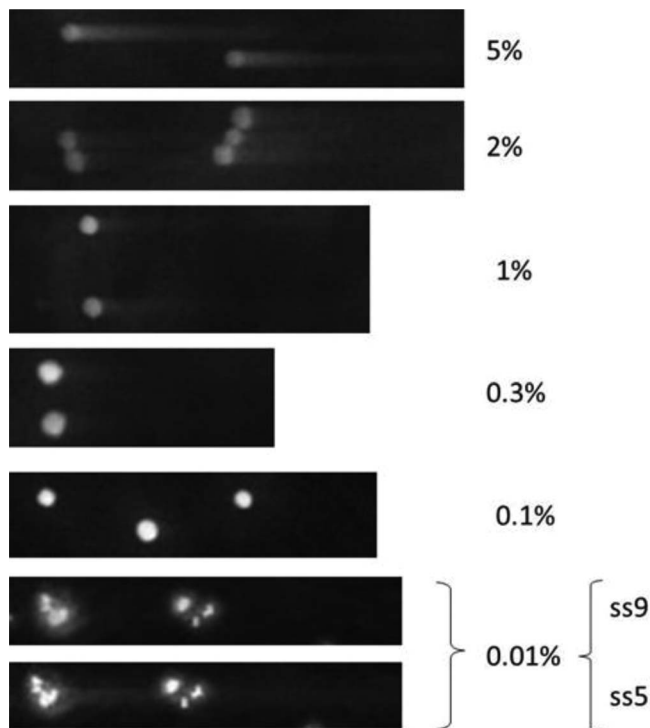| $^5D_0 \rightarrow ^7F_2$ (C_2) 611 nm	$^5D_0 \rightarrow ^7F_{1a}$ (S_6) 582 nm	$^5D_1 \rightarrow ^7F_1$ (C_2) 533 nm	Not specified	Remark	Ref.
1.76				PL	15
1.2				PL: YAG-Nd 532nm	16
0.96	6.9	0.09 1)		PL: 0.01% Eu	8
			1.1	CL: 4keV	26
1.1	7.9			PL	7
			1.2	CL: 1kV and 1µA/cm²	10
		0.08		CL: 4kV 4.6%Eu	27
0.97	5.5	< 0.05		CL: 15kV 0.1%Eu	This work

Figure 12. CL-micrographs of Y_2O_3:Eu^{3+} nanospheres with various Eu^{3+} concentrations at 10keV. Dwell time of the E-beam on one sphere is 260 μs. For the 0.01% Eu^{3+} sample the magnification is smaller. For the image of scan speed 9 (ss9) the dwell time is 40 μs and for ss5 it is 2.5 μs.

is 2 nm and the current is about 1nA in the FESEM. This yields a current density at the position where the beam hits the phosphor of 3×10^4 A/cm². This current density is so high that Y_2O_3:Eu^{3+} will hardly emit any light, contrary to what is observed in Figures 11 and 12. Thus, the effective current density must be lower and its value can be estimated by considering the interaction volume of the E-beam in the phosphor.

In the FESEM the E-beam dwells for a short time Δt on the Y_2O_3:Eu^{3+} nanoparticles having a diameter of 225 nm, which corresponds to a cross section of 4×10^{-10} cm². In other words, the effective current density hitting the particle is 2.5A/cm². The interaction volume of a narrow electron beam of 10keV impinging on a nanoparticle of 225nm is depicted in Figure 13. This shows a simulation result generated with the Casino software package, made and described by Drouin et al.[28] This package yields electron trajectories in a solid by a Monte Carlo algorithm. The essential output shown in Figure 13 is the interaction volume in a large crystal of Y_2O_3, much larger than the dimension of one spherical nanoparticle of 225 nm. The effect of the denser Eu^{3+} may be neglected in these simulations. The cross section of the interaction volume is taken at the contour line of 95% absorbed energy. This interaction volume is much larger than the volume of one nanoparticle: therefore, a substantial fraction of the E-beam energy is

Table IV. Time constants of individual Y_2O_3:Eu^{3+} nanoparticles evaluated by ImageJ from CL-micrographs.

Concentration Eu^{3+} (%)	τ (ms)
10	0.8
5	0.9
2	0.5
1	0.4
0.5	0.2
0.3	0.3

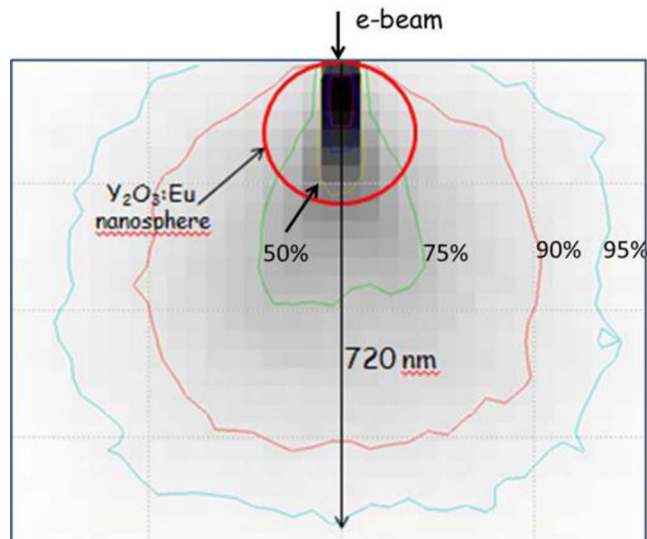**Figure 13.** Casino simulation of electron trajectories in Y_2O_3:Eu^{3+}. E-beam energy 10keV. The volumes inside the contour lines have absorbed the indicated irradiated electron energy. The dimension of the nanospheres used in this work has been overlaid in the diagram to facilitate comparison.

not absorbed by the Y_2O_3:Eu^{3+} nanoparticle at 10keV. The contour line of 50% absorption is just within the dimensions of the nanoparticles used in this work, and thus slightly more than 50% of the electron energy is expected to be absorbed in the nanoparticle, if it were struck centrally (as shown) and less if it were struck to one side. From this consideration it can be concluded that the effective current density for the Y_2O_3:Eu^{3+} nanoparticles in the FESEM is approximately $0.5 \times 2.5 = 1.25$A/cm²: this is still more than 6 orders of magnitude larger than the current density in the experiments described in the section on luminous efficiency and emission decay.

Klaassen et al.[8] measured the CL saturation of transitions from the $^5D_0$ (C₂) and $^5D_1$ (C₂) levels for Y_2O_3:Eu^{3+} with 1% Eu^{3+} as a function of current density between 1×10^{-6} and 1×10^{-2} A/cm² under stationary conditions. Figure 14 is a double log plot of the relative efficiencies of the dominant $^5D_0$ -$^7F_2$ (C₂) transition at 611nm and the fast decaying $^5D_1 \rightarrow {}^7F_1$ (C₂) transition at 533 nm for Y_2O_3:Eu^{3+} with a Eu^{3+} concentration of 1%, according to Klaassen et al.[8] The curves at j>1×10^{-2} A/cm² are extrapolations from the data of Klaassen et al. Point F in the plot indicates the effective current density for
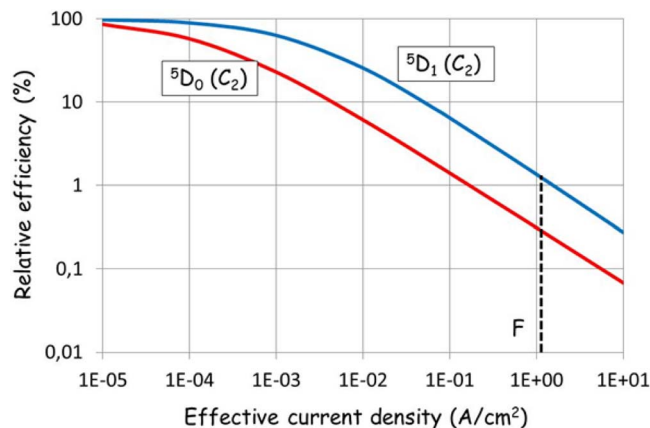

Figure 14. Relative CL-efficiency of two transition types in Y_2O_3:Eu^{3+} (1% Eu^{3+}) versus current density under stationary excitation conditions according to Klaassen et al.[8] Point F on the horizontal axis marks the effective current density in the FESEM for one particle; it is located outside the measuring range of Klaassen et al.

one Y_2O_3:Eu^{3+} nanoparticle in the FESEM. It can be seen that under stationary conditions the efficiency of the $^5D_0 \rightarrow {}^7F_2$ (C_2) peak is only 0.3% of the efficiency at low current density (1μA/cm^2), while the efficiency of the $^5D_1 \rightarrow {}^7F_1$ (C_2) transition is still 1.2% of its value at 1μA/cm^2.

Klaassen et al.[8] also measured the current density $j_{50\%}$ at which the relative efficiency is 0.5 for various concentrations of Eu^{3+}. At stationary conditions they found that $j_{50\%}$ varied only by a factor of 2 for a concentration change of a factor of 20. In other words, $j_{50\%}$ is rather insensitive to the Eu^{3+} concentration. Stationary conditions are defined by the inequality $\Delta t/\tau > 1$: this holds for the $^5D_1 \rightarrow {}^7F_1$ (C_2) transition at 533nm with $\tau \approx 50$ μs in the normal scanning conditions of the FESEM, whereas we have $\Delta t/\tau < 1$ for the $^5D_0 \rightarrow {}^7F_2$ (C_2) transition at 611nm. Thus the application of the Klaassen et al. data for our FESEM experiments is not completely justified for the 611 nm transition. Nevertheless, it is assumed that the relative efficiency of this transition in the FESEM at $\Delta t=260\mu$s is only a little bit larger than under stationary conditions as represented in Figure 14.

In spite of this uncertainty, it can be concluded that Figure 14 provides a satisfactory explanation of the CL-micrographs in Figure 12: at low Eu^{3+} concentrations the light output for the $^5D_0-{}^7F_2$ (C_2) transition virtually disappears, whereas the fast decaying $^5D_1 \rightarrow {}^7F_1$ (C_2) transition is still emitting light. The consequence is that the horizontal tails in Figure 12 disappear at low Eu^{3+} concentration, because the (very short) decay tail of the $^5D_1 \rightarrow {}^7F_1$ (C_2) transition is hidden by the halo effect around the particles. It should be kept in mind that Figure 14 refers to relative efficiency, whereas Figure 12 refers to a greyscale being proportional to the total light output. Figure 14 also explains the decrease of the decay time of Y_2O_3:Eu^{3+} for low Eu^{3+} concentrations in Table IV, because the contribution of the $^5D_0$ levels in the decay phenomenon is almost disappearing, so that the effect of fast decaying ^5D_J levels becomes clearer. As mentioned in the experimental section, the CL-detector in the FESEM was panchromatic; so, we could not record spectra of individual Y_2O_3:Eu^{3+} nanoparticles at high current density. We plan to do this in the future.

Conclusions

The results obtained in this CL study of monosized spherical nanoparticles Y_2O_3:Eu^{3+} largely confirm the work on micrometer sized Y_2O_3:Eu^{3+} published between 1970 and 1995.

One clear difference is the luminous efficiency, which is about 30% lower for the nanoparticles than that of micrometer sized particles.

We have presented a new theory that enables a straightforward evaluation of the critical distance for radiationless energy flow from Eu^{3+} ions in S_6 sites to Eu^{3+} ions in C_2 sites. This evaluation requires recording of CL spectra at various Eu^{3+} concentrations at room temperature.

From the explanation of the results we have discussed above we find no evidence for a none statistical preference of Eu^{3+} for either of the crystallographic sites in cubic Y_2O_3:Eu^{3+}.

From the detailed analysis of the decay of the $^5D_0 \rightarrow {}^7F_2$ (C_2) transition at 611 nm and $^5D_0 \rightarrow {}^7F_1$ (S_6) transition at 582 nm it was found that the interaction between excited Eu^{3+} ions varies with the inverse of the sixth power of the Eu^{3+} : Eu^{3+} distance indicating that this type of interaction has a dipole-dipole nature.

Furthermore, we have shown that the interpretation of FESEM CL-micrographs of Y_2O_3:Eu^{3+} nanoparticles was possible due to the detailed information that was published on the saturation and decay behavior. Conversely it can be concluded that CL-microscopy offers opportunities to generate new information on (nanostructured) phosphors.

References

1. D. den Engelsen, P. G. Harris, T. G. Ireland, R. Withnall, and J. Silver, *ECS J. Solid State Sci. Technol.*, **2**, R201 (2013).
2. D. den Engelsen, P. G. Harris, T. G. Ireland, and J. Silver, *ECS J. Solid State Sci. Technol.*, **3**, R53 (2014).
3. P. Harris, D. den Engelsen, T. Ireland, G. Fern, and J. Silver, *Proceedings of ICOOPMA* (2014).
4. J. Heber, K. H. Hellwege, U. Köbler, and H. Murmann, *Z. Physik*, **237**, 189 (1970)
5. R. G. Pappalardo and R.B. Hunt, *J. Electrochem. So*c., **132**, 721 (1985).
6. R. B. Hunt and R. G. Pappalardo, *J. Lumin.*, **34**, 133 (1985).
7. M. Buijs, A. Meyerink, and G. Blasse, *J. Lumin.*, **37**, 9 (1987).
8. D. B. M. Klaassen, R. A. M. van Ham, and T. G. M. van Rijn, *J. Lumin.*, **43**, 261 (1989).
9. D. B. M. Klaassen, T. G. M. van Rijn, and A. T. Vink, *J. Electrochem. Soc.*, **136**, 2732 (1989).
10. H. Bechtel, W. Czarnojan, M. Haase, W. Mayr, and H. Nikol, *Philips. J. Res.*, **50**, 433 (1996).
11. S. Yang, J. A. Cooper, C. Stoffers, F. Zhang, J. Penczek, B.K. Wagner, S. M. Jacobsen, and C. J. Summers, *Extended abstracts of the second international conference on the science and technology of display phosphors*, November 18–29, San Diego, CA, 255 (1996).
12. K. Ohno in "*Phosphor Handbook*", Chapter 6, Edited by W. Yen, S. Shionoya, and H. Yamamoto, 2nd ed., CRC-Press, Boca Raton (2007).
13. X. Jing, T. Ireland, C. Gibbons, D. Barber, J. Silver, A. Vecht, G. Fern, P. Trogwa, and D. Morton, *J. Electrochem. Soc.*, **146**, 4654 (1999).
14. Y. D. Jiang, Z. L. Wang, F. Zhang, H.G. Paris, and C. J. Summers, *J. Mater. Res.*, **13**, 2950 (1998).
15. S. Ray, P. Pramanik, A. Singha, and A. Roy, *J. Appl. Phys.*, **97**, 094312 (2005).
16. G. Jia, M. Yang, Y. Song, H. You, and H. Zhang, *Cryst. Growth Des.*, **9**, 301 (2009).
17. Y. Chung, S. Park, K. Jang, I. Kim, Y. I. Lee, and H. J. Seo, *J. Korean Phys. Soc.*, **42**, 543 (2003).
18. M. I. Martinez-Rubio, T. G. Ireland, G. R. Fern, J. Silver, and M. J. Snowden, *Langmuir*, **17**, 7145 (2001)
19. P. A. Tanner, L. Fu, and B-M. Cheng, *J. Phys. Chem. C*, **113**, 10773 (2009).
20. E. Antic-Fidancev, J. Hölsä, and M. Lastusaari, *J. Phys.: Condens. Matter*, **15**, 863 (2003).
21. J. Silver and R. Withnall, *Chem. Rev.* **104**, 2833 (2004).
22. G. Schaack and J. A. Koningstein, *J. Opt. Soc. Am.*, **60**, 1110 (1970).
23. J. Silver, T. G. Ireland, and R. Withnall, *J. Electrochem. Soc.*, **151**, H66 (2004).
24. J. B. Talbot, E. Slusky, and S.K. Kurinec, *J. Mater. Sci.*, **39**, 771 (2004).
25. S. Qiang, C. Barthou, J. P. Denis, F. Pelle, and B. Blanzat, *J. Lumin.*, **28**, 1 (1983).
26. J. Thomes, C. Seager, D. Tallant, and P. Holloway, *Extended abstracts of the sixth international conference on the science and technology of display phosphors*, November 6–8, San Diego, CA, 249 (2000).
27. C. H. Seager, D. R. Tallant, M. Hampden-Smith, and D. Skamser, *Extended abstracts of the fifth International conference on the science and technology of display phosphors,* November 8–10, San Diego, CA, 321 (1999).
28. D. Drouin, A. R. Couture, D. Joly, X. Tastet, V. Aimez, and R. Gauvin, *Scanning*, **29**, 92 (2007).